Acquiring and Reconstructing an Image Volume

Tissue Sample Preparation

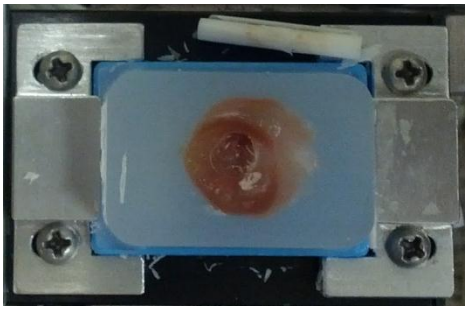

Figure 1: Guinea pig heart embedded in paraffin

A rodent heart (usually mouse or guinea pig) is rapidly excised from the sedated animal and perfused on a Langendorf apparatus with a Tyrodes solution[1]. The heart is allowed to stabilize for 20 minutes from the start of perfusion. In order to create metabolic sinks, global ischemia is induced in the heart by halting perfusion for 30 minutes[2]. Following this period of ischemia, the perfusion is restored with a normal Tyrodes perfusate for 5 minutes. This is a period of mitochondrial membrane dynamics[3]. The perfusate is then switched to a Tyrodes containing 2 µM Mitrotacker Red CMXRos and 20 µg/mL Hoechst. This solution is recirculated through the apparatus for 10 minutes so that all nuclei and polarized mitochondria are labeled. The perfusate is changed back to the normal Tyrodes for 5 minutes to washout any unattached fluorophores. The heart is then fixed with methanol chilled to -20 C, and embedded in paraffin.

Imaging the Sample

The paraffin embedded sample is mounted to the Automated Volume Imaging Machine (AVIM). The AVIM interfaces with a Zeiss 7MP two-photon microscope, an imaging modality that can acquire discrete planes in z deep into the tissue. Figure 2 demonstrates the automated acquisition process. The AVIM initially positions the sample beneath the microscope objective so than an area of the sample can be imaged, 850 µm by 850 µm for a 10X objective but more generally *a* by *a* pixels. The focal plane of the objective is adjusted so that several images are acquired at discrete increments of *z* for this single *x* and *y* coordinate of the sample deep into the sample. Typically, this depth is limited to approximately 70 µm in cardiac tissue before photon scattering and absorption degrades image quality. This is the calculated depth of the focal plane that takes into account the refractive index mismatch between the air immersion objective (n = 1.0) and the paraffin-embedded sample (n = 1.47)[4]. The collection of images at different *z* values for a particular *x* and *y* coordinate is referred to as an optical stack. Following the acquisition of an optical stack, the

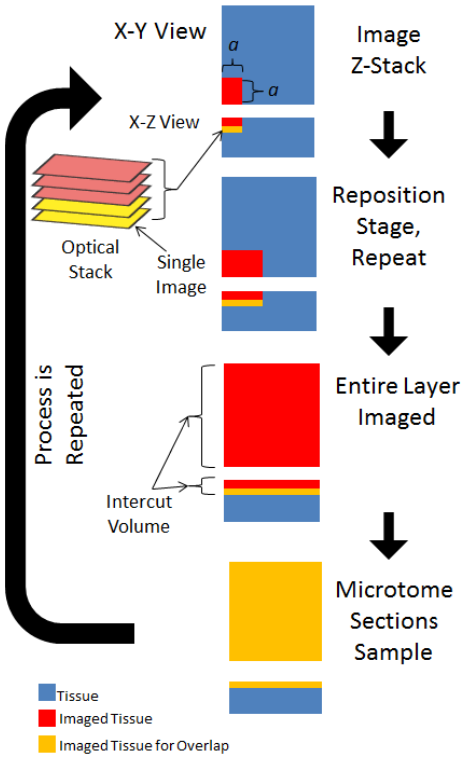

Figure 2: Image acquisition process. Individual optical stacks are collected at each position over the surface of the sample. The sample is sectioned with a microtome, leaving a portion of the sample imaged prior. Then the process is repeated until complete.

AVIM repositions the sample beneath the objective so that an optical stack is collected over an adjacent area of the sample, overlapping approximately 10% of the prior image area. This process of positioning the sample and collecting an optical stack is repeated until the sample's surface has been imaged in its entirety. This collection of optical stacks over the surface of the sample is referred to as an intercut volume. The AVIM then removes the sample from beneath the objective. The height of the sample is adjusted relative to a nearby microtome blade so that a portion of the sample can be sectioned off when an actuator drives the sample under the blade. The portion of the sample removed is less than the portion imaged (depth of optical stack is greater than the cut depth). The previously imaged portion of the sample remaining will be imaged again as a reference for image registration performed later. The sample is then returned to the objective to repeat the process of imaging the exposed surface, i.e. collecting another intercut volume. By repeating this as many times as needed, the sample can be imaged in its entirety. The AVIM can image samples as large as 20 mm in each dimension.

The actuator needed for the microtome sectioning introduces some error in the coordinates between cuts. This is minimized by introducing a positive stop in the return of the actuator travel to define the imaging position, resulting in less than 20 µm error between cuts as compared to almost 200 µm when using the fully retracted position of the actuator as the imaging position. The correction of the actuator-induced error is described in the reconstruction methodology.

Image Volume Reconstruction

In-Plane Correction - Removing Vignettes

With the offsets of the intercut volumes determined, the necessary coordinates are known to reconstruct the images into an image volume. However, the two-photon imaging modality creates certain image artifacts that can be corrected, mainly image vignetting and signal attenuation with increasing imaging depth. Image vignetting is removed with an algorithm developed by Chow et al.[5] Figure 3 demonstrates how for a given *z* coordinate, all images in that plane are stacked. Then the average value and minimum value is determined for each *x*,*y* coordinate within the images. This produces an "average" image I_B where the individual pixels for that image are the average value calculated for those coordinates from the image stack and a "minimum" image I_M with the corresponding minimum values for each pixel coordinate. Both the "average" image and the "minimum" image are Gaussian filtered to remove any image specific trends. Next, the values stored in the filtered "average" and "minimum" images are used in Equation 1 to correct each image in the plane separately.

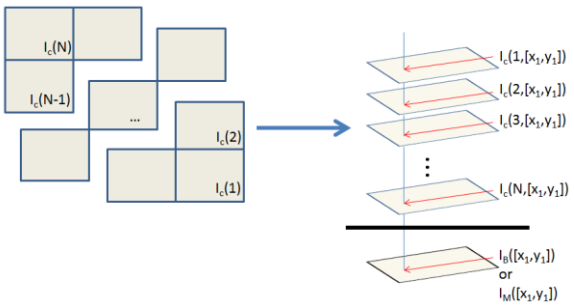

Figure 3: In-plane image correction by Chow et al. For a given z, all images in that plane are stacked, and an average (B) and minimum (M) value is calculated for each x,y coordinate within the images.

$$I_O(n,[x,y]) = \overline{(I_B - I_M)}\left(\frac{I_c(n,[x,y]) - I_M([x,y])}{I_B([x,y]) - I_M([x,y])}\right) \quad (1)$$

Where I_C is the collected image, and I_O is the corrected image. This process of calculating an "average" and "minimum" image for in-plane image correction is repeated throughout the collected volume.

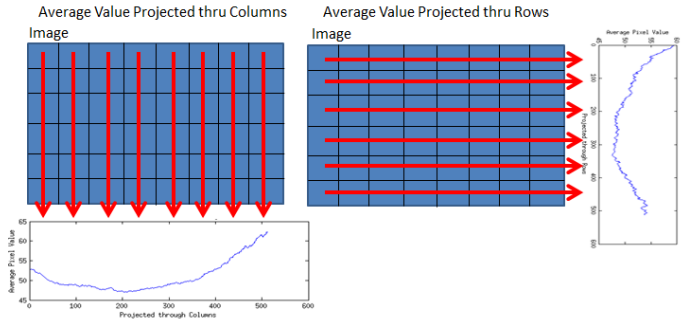

Figure 4: Creating x and y profiles of pixel intensity. Hovhannisyan et al. 2008

A second in-plane correction algorithm developed by Hovhannisyan et al.[6] was considered. Their method takes the "average" image as described above and projects average pixel values in the x and y directions, plotting the x and y pixel intensity profiles for the "average" image. Figure 4 demonstrates this process and includes representative data. A quadratic function is fit to the *x* and *y* profiles. The images are then multiplied by the inverse of these quadratic functions. This method was compared to the Chow algorithm described above using the x and y profiles as a metric of how well the correction algorithm performed. A perfectly flat x and y pixel intensity profile was assumed to be the theoretical ideal correction result. This comparison was done across several datasets, and the Chow algorithm brought the x and y profiles closest to ideal in all cases (Table 1).

Table 1: Chow vs Hovhannisyan comparison

	Dataset 1		Dataset 2		Dataset 3	
	X-profile Error	Y-profile Error	X-profile Error	Y-profile Error	X-profile Error	Y-profile Error
Raw Data	15.59	7.37	0.64	0.52	0.79	4.34
Chow	2.23	1.13	0.001	0.001	0.002	0.01
Hovhannisyan	3.79	2.84	0.049	0.076	0.25	0.12

Image Stitching – Creating Image Slices

Following in-plane image correction, individual images for a particular *z* value are rigidly stitched into a single image. This stitched image for a single *z* value is referred to as an image slice. Each intercut volume (except for the topmost and bottommost volume) will have images at the top and bottom of the *z* range that have been imaged twice, see Figure 6. In these overlapping regions, both sets of images collected will be stitched for image registration done later; however, the images at the top of the optical stack rather than the corresponding images at the same *z* value at the bottom of the optical stack will be used in the final image volume. This is done for two reasons: 1) while the signal attenuation with depth will be corrected for, this is not a perfect correction, and the lower images in an optical stack will be somewhat dimmer than the top of the stack, and 2) the point spread function will increase with imaging depth, meaning the images closer to the surface will have better

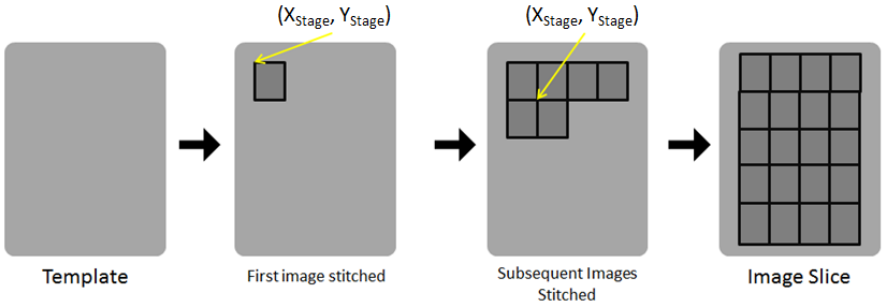

Figure 5: Stitching individual tiles into image slices based on stage coordinates.

image quality than the deeper images.

Figure 5 demonstrates the stitching process. A blank template is created large enough for the amount of pixels collected at a z value as well as the amount of offset that has to be taken into account due to the actuator-induced error. For the topmost intercut volume, the coordinate system is centered on the stitching template. Each image acquired at the initial *z* value is stitched onto the template at the coordinates recorded during its acquisition. During acquisition, there is an overlap of the images acquired over the surface of the sample. As described above, the edges of each tile can have a vignette or fall off in intensity towards the edge of the tile. Although this is corrected for with the in-plane correction algorithm, further improvements in stitched image quality can be achieved by clipping the edges of the tiles. For a 10% overlap in the *x* and *y* dimension, this means 5% of each dimension can be trimmed off each edge of the tile (excluding the perimeter tiles). Once all images for that *z* value have been clipped (where appropriate) and stitched onto the template, the resulting image is saved and the template is cleared. This is repeated until an image slice has been output for each value of *z* in the image volume.

Image Registration - Aligning Images Between Cuts

To determine the actuator-induced error between intercut volumes, the portion of the sample imaged twice (before and after the cut) will be registered with itself. The image slice stitched at the bottom of the optical stack before the cut is registered to the corresponding image slice (same *z* coordinate) after the cut as shown in Figure 6. The two image slices are registered with a Nelder Mead Simplex algorithm[7] adjusting the *x*,*y* offset of the second-imaged area with respect to the first in order to maximize the cross-correlation of the overlapping areas, a registration method robust to differences in image intensity[8]. The *x*,*y* offsets are determined in this way for each error-inducing step (sectioning of the sample). The offset found is the error between the two intercut volumes being registered. In order to bring all of the intercut volumes into the same frame of reference, each offset is added to the preceding offset value starting at the top of the image volume and working down. Once the offsets between each intercut volume are determined, the stitched image slices are adjusted on their templates to bring the image slices into alignment.

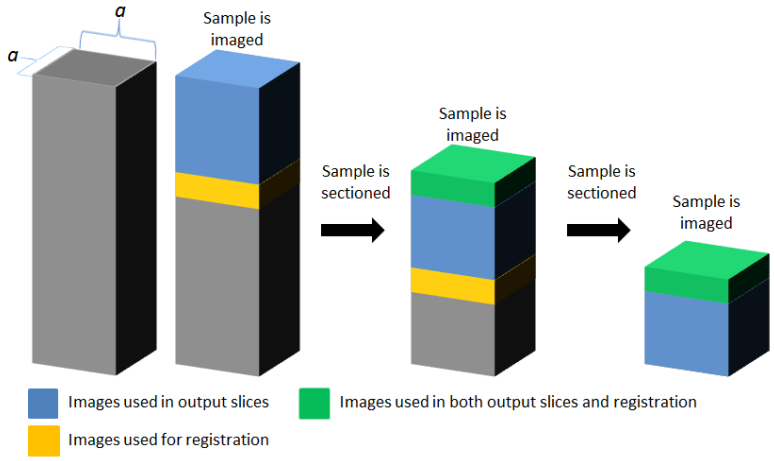

Figure 6: Column representing the imaging and cutting of a single image area throughout the depth of the sample. The three cases of the top of the sample, middle of the sample, and bottom of the sample are demonstrated as to their contributions to the image reconstruction process

Out-of-plane Image Correction - Intensity Attenuation Compensation

The signal attenuation, or dimming, with depth is a result of scattering and absorption both of the incident and reflected photons. Images acquired from deeper in the sample will be dimmer than those

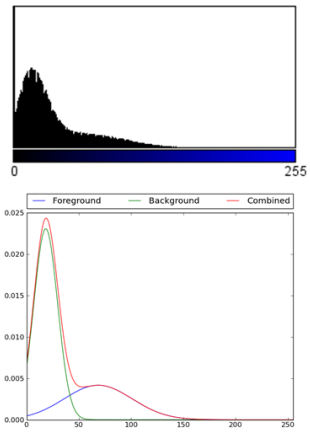

Figure 7: Fitting two Gaussian distributions to the foreground and background components of the image histogram. These parameters are used to correct for signal attenuation with depth according to Gopinath et al.

acquired closer to the surface. Many approaches have been developed to remove this affect from two-photon microscopy images. Because of the large depth of the optical stacks collected by the AVIM, it was necessary to have a correction method that was robust and insensitive to the noise that is inherent in images acquired at large depths. After testing several algorithms, a mixture-modeling algorithm developed by Gopinath et al.[9] was found to work the best. The algorithm takes an intercut volume and labels the brightest image slice the reference image, usually the top image slice. It then assumes the image has two components in its histogram, a foreground component and a background component. The expectation-maximization algorithm is used to fit a Gaussian distribution to each of these components in the histogram of the reference image. An example of this is shown in Figure 7. This process is repeated for the other images in the optical stack. The non-reference images are then adjusted according to Equation 2 so that the parameters of their foreground and background components more closely resemble those of the reference image. In this equation, x' is the compensated intensity image stack (*n*th pixel, *j*th image), F is the membership probability for the background (denoted as *1*) and the foreground (denoted as *2*), μ is the mean of the corresponding Gaussian with σ as its standard deviation, and the subscript *r* corresponds to the reference image. This process is carried out on each intercut volume collected.

$$(x')_n^j = F_2^j(n) \cdot \left\{ \frac{\left(x_n^j - \mu_2^j\right)}{\sigma_2^j} \sigma_r + \mu_r \right\} + F_1^j(n) \cdot x_n^j \qquad (2)$$

In deciding on the algorithm by Gopinath et al., two other algorithms were considered. Guan et al. 2008 developed an algorithm that fit the pixel intensity attenuation with depth to an exponential decay, a model suggested by the Lambert-Beer Law[10]. And Lee et al. 2006 developed an algorithm referred to as a mean-weight filtering technique[11]. The algorithms were evaluated based on their ability to restore pixel intensity with increasing depth as well as preserve image specific features. In regards to preserving pixel intensity with depth, Lee's mean-weight filtering technique outperformed all others; however the

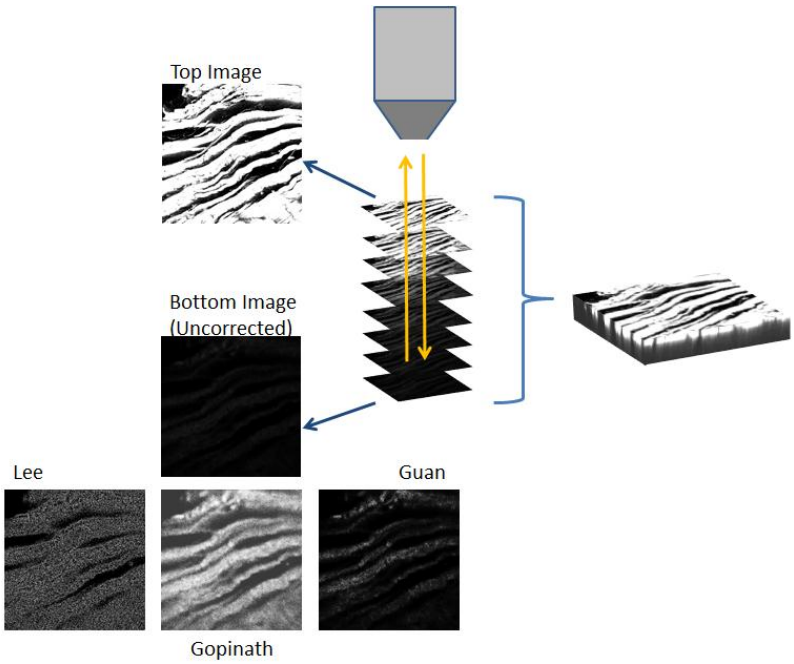

Figure 8: Comparison of depth attenuation correction techniques.

resulting corrected images were so noisy as to obscure the relevant structures of interest. An example is shown below in Figure 8. Of the two remaining algorithms, Gopinath's mixture modeling algorithm was superior in both restoring pixel intensity (an objective measure) as well as preserving image quality (a subjective measure).

It should be noted that the algorithms considered for correcting pixel intensity attenuation with increasing depth were originally designed and evaluated on optical stacks ranging from 10-15 µm. Our application to a range of 70 µm and the inherently large light scattering effect of cardiac tissue being imaged in our work created a more significant attenuation than originally considered in the design of these algorithms.

Resulting Reconstructed Image Volume – The Output

The output of the image reconstruction process is a set of image slices saved as individual PNG files and a parameters file specifying the resolution in and between these images. These can be loaded into various image visualization programs for analysis.

1. Brown Da, Aon Ma, Frasier CR, Sloan RC, Maloney AH, Anderson EJ, O'Rourke B. Cardiac arrhythmias induced by glutathione oxidation can be inhibited by preventing mitochondrial depolarization. *Journal of molecular and cellular cardiology*. 2010;48:673-679
2. Slodzinski MK, Aon Ma, O'Rourke B. Glutathione oxidation as a trigger of mitochondrial depolarization and oscillation in intact hearts. *Journal of molecular and cellular cardiology*. 2008;45:650-660
3. Lyon AR, Joudrey PJ, Jin D, Nass RD, Aon Ma, O'Rourke B, Akar FG. Optical imaging of mitochondrial function uncovers actively propagating waves of mitochondrial membrane potential collapse across intact heart. *Journal of molecular and cellular cardiology*. 2010;49:565-575
4. Cooper PR. Refractive-index measurements of paraffin, a silicone elastomer, and an epoxy-resin over the 500-1500-nm spectral range. *Appl Optics*. 1982;21:3413-3415
5. Chow SK, Hakozaki H, Price DL, MacLean NA, Deerinck TJ, Bouwer JC, Martone ME, Peltier ST, Ellisman MH. Automated microscopy system for mosaic acquisition and processing. *J Microsc*. 2006;222:76-84
6. Hovhannisyan Va, Su P-J, Chen Y-F, Dong CY. Image heterogeneity correction in large-area, three-dimensional multiphoton microscopy. *Optics express*. 2008;16:5107-5117
7. Nelder JA, Mead R. A simplex-method for function minimization. *Comput J*. 1965;7:308-313
8. Rosenfeld A. *Digital picture processing*. Orlando, FL: Academic Press; 1982.
9. Gopinath S, Wen Q, Thakoor N, Luby-Phelps K, Gao JX. A statistical approach for intensity loss compensation of confocal microscopy images. *J Microsc*. 2008;230:143-159
10. Guan Y, Cai Y, Zhang X, Lee Y, Opas M. Adaptive correction technique for 3d reconstruction of fluorescence microscopy images. *Microsc Res Techniq*. 2008;71:146-157
11. Lee SC, Bajcsy P. Intensity correction of fluorescent confocal laser scanning microscope images by mean-weight filtering. *J Microsc*. 2006;221:122-136